

Solution Annealing of Super Duplex Stainless Steel: Correlating Corrosion Performance with Grain Size and Phase-Specific Chemistry



RIYA MONDAL, A. RAJAGOPAL, SUNIL KUMAR BONAGANI, ADITYA PRAKASH, D. FULORIA, P.V. SIVAPRASAD, G. CHAI, V. KAIN, and I. SAMAJDAR

A super duplex stainless steel was subjected to solution annealing at 1323 K. This led to grain coarsening, 'limited' (~ 7 pct by area) austenite-to-ferrite phase transformation and changes in phase-specific chemistry. No changes in the phase boundary nature or galvanic coupling between phases were, however, noted. The general corrosion behavior was determined by the electrochemical performance of the individual phases. The corrosion performance of the ferrite phase degraded monotonically with annealing time. This was related to a combined effect of grain coarsening and dilution in alloying (chromium and molybdenum content) elements. Corrosion of the austenite phase was, however, non-monotonic: as the effects of grain coarsening was counter-balanced, at least during the initial stages of annealing, by relative molybdenum enrichment. This study thus provided clear experimental data relating phase-specific corrosion performance with annealing induced changes in grain size and local chemistry in a super duplex stainless steel.

<https://doi.org/10.1007/s11661-020-05672-w>

© The Minerals, Metals & Materials Society and ASM International 2020

I. INTRODUCTION

DUPLEX stainless steels (DSS) offer a combination of excellent corrosion resistance and mechanical properties.^[1–3] The corrosion resistance and mechanical properties of DSS are even better than that of the austenitic stainless steels, and are attributed to the typical two-phase microstructure.^[1,2,4,5] Like the austenitic stainless steels, DSS is also solution annealed at 1323 K to 1423 K (1050 °C to 1150 °C) and for appropriate durations.^[1,4] Though the solution annealing in DSS serves the purpose of dissolving unwanted phases^[1,4,6]; it is often associated with grain coarsening, possible austenite-to-ferrite phase transformation and changes in the phase-specific chemistry.^[1,6–11] Naturally, such changes in the microstructures are expected to reflect on the corrosion performance.

The excellent corrosion performance of a stainless steel is related to the overall passivation: the formation of chromium oxide film.^[12,13] This chromium oxide passive film imparts uniform corrosion resistance. The local breakdown(s) of the passive films, on the other hand, accounts for degradation in the corrosion behavior.^[12–14] The DSS grades, for example, are often categorized by their pitting resistance equivalent number (PREN).^[1,2,4,6] The PREN is a measure of the local breakdown(s) in the passive film under pitting environment. The chemistry (more specifically the chromium (Cr), molybdenum (Mo) and nitrogen (N) content) of the alloy decides the PREN.^[1,2,11,12,15] However, there are enough examples^[8,10,11,16–20] in the literature showing that pitting corrosion resistance, especially the critical pitting temperature,^[8,16–18] depends on the substrate microstructure as well. More specifically, the grain size refinement is expected to enhance corrosion performance^[21–24]; a combined effect of the nature^[21,24] and electronic properties (donor-acceptor densities)^[17,24,25] of the oxide film. The alloying of the substrate is also important. The exact chemistry of the substrate may affect the stability or retention of the oxide film.^[26–36] The protective ability of the oxide film on duplex^[26,33–35] and austenitic^[27–32,36] stainless steels is reported to depend on the chromium and molybdenum contents.

RIYA MONDAL, ADITYA PRAKASH, D. FULORIA, and I. SAMAJDAR are with the Department of Metallurgical Engineering & Materials Science, Indian Institute of Technology Bombay, Powai, Mumbai 400076, India. Contact e-mail: indra@iitb.ac.in A. RAJAGOPAL, P.V. SIVAPRASAD, and G. CHAI are with Sandvik Materials Technology, 811 81 Sandviken, Sweden. SUNIL KUMAR BONAGANI and V. KAIN are with the Materials Processing and Corrosion Engineering Division, Bhabha Atomic Research Centre, Trombay, Mumbai 400085, India.

Manuscript submitted September 12, 2019.

Article published online February 18, 2020

The solution annealing, and associated microstructural evolution, thus may affect the (uniform) corrosion behavior. And there are several excellent research publications [8,10,11,16–20] relating solution annealing with pitting and general corrosion. However, focused research was never extended to (i) phase-specific electrochemical performance and (ii) relating (i) with local microstructure. These defined the twin objectives of the present manuscript.

II. EXPERIMENTAL PROCEDURE

This study involved solution annealing of a super duplex stainless steel: a Sandvik™ SAF-2906™ grade. In duplex stainless steel (DSS), the solution annealing temperature is often grade specific.^[1] The standard and super DSS grades require ~ 1323 K to 1343 K (1050 °C to 1070 °C) for solution annealing. It is to be noted that 1323 K is the most commonly used^[1–6] solution annealing heat treatment for this specific grade (SAF2906), and the same was used in the present study. Further, different solution annealing periods, 1 to 12 hour, were used. The very high-solution annealing time periods are of ‘limited’ relevance to actual industrial practice. However, exposure to such long periods stimulate accelerated microstructural evolution, which is of relevance to harsh service environment. This study had twin objectives: (i) role of solution annealing time of microstructural evolution and (ii) extend such microstructural evolution to relative corrosion performance.

Direct *ex-situ* observations, with electron backscattered diffraction (EBSD) and wavelength-dispersive X-ray spectroscopy (WDS), helped in identifying the phase-specific but time-dependent microstructural changes. Such changes included grain coarsening, austenite-to-ferrite phase transformation and changes in the phase-specific chemistry. The last two factors were also simulated with a commercial diffusion software DICTRA™. The samples were then subjected to selective dissolution of the austenite or the ferrite phases. Phase-specific dissolution data and single-phase electrodes were thus obtained. Subsequent observations, on single-phase electrochemical behavior, were further collaborated with local information from Fourier-transformed infrared spectroscopy (FTIR) imaging, providing information on the local stability or retention of the passive chromium oxide. Experimental procedures are further explained in following paragraphs.

A. Sample Preparation and Microstructural Characterization

A super duplex stainless steel (Sandvik SAF-2906™), chemical composition listed in Table I, was procured as a commercial 12-mm-thick hot rolled plate. Samples (15 mm × 15 mm × 3 mm) were taken from the mid-thickness and mid-width sections, of the hot-rolled plates, by electro-discharge machining. Further preparation involved standard metallography (grinding on successively finer SiC papers up to 1200 grit and then polishing

with ~ 0.5 μm diamond paste) plus electropolishing. For the latter, an electrolyte of methanol and perchloric acid (80:20) was used at 253 K (– 20 °C) and 16 volts dc. These electropolished specimens were then solution annealed, with resistance heating plus protective environment, in a deformation simulator Gleeble™ 3800. A temperature of 1323 K (1050 °C) and different durations (1, 3, 6, 8 and 12 hours) were used, followed by water quenching.

To compare microstructures of the same regions, before and after the solution annealing, micro-hardness indentations were made. The same area on the specimen (bound by 4 indentations) was examined by the EBSD (electron backscattered diffraction) and WDS (wavelength-dispersive X-ray spectroscopy) before and after the solution annealing. A Fei™ Quanta-3d FEG (field emission gun) SEM (scanning electron microscope) with EDAX™ EBSD (OIM™) and WDS was used. It is to be noted that the WDS used TEX™ version, involving poly-capillary lens and parallel beam spectrometry. Beam and video conditions were kept identical between the measurements.

B. Electrochemical Tests

The electrochemical tests included: (I) General Corrosion behavior with Potentiodynamic Polarization (used for specimens with both austenite and ferrite phases) and (II) Phase-Specific Electrochemistry. (I) is the standard^[37] potentiodynamic polarization, while (II) involved rigorous procedure for preparation on single-phase electrodes^[38–46] and then testing them for potentiodynamic polarization, electrochemical impedance spectroscopy (EIS) and Mott–Schottky (M–S) analysis.^[41,42,47] Two different electrochemical environments were used. The former (1M H₂SO₄ solution) was used for general corrosion including passivation, while 2 M H₂SO₄ + 0.5 M HCl was used for phase-specific electrochemistry which is selective dissolution of the respective phases). It is to be noted that the selection of the electrochemical environment was based on the past literature,^[38–48] and multiple trials (which has not been included for brevity). Following are the details on the experimental procedures adopted.

C. General Corrosion Behavior with Potentiodynamic Polarization

This was carried out in 1 M H₂SO₄ solution (scan rate of 20 mV/min) at an ambient temperature. A freshly prepared solution was used for each test. All the tests were performed using VSP-300™ potentiostat: a platinum electrode as the counter electrode, a saturated calomel electrode (SCE) as the reference electrode and the specimen as the working electrode. The test solution was deaerated by purging Ar gas: ~ 30 minutes before the start of the test and also during the test. At the start of each electrochemical experiment, the specimen was polarized at – 1 V_{SCE} for 60 seconds. This was followed by dipping in the solution for 30 minutes to obtain a stable open circuit potential (OCP). The tests were conducted by scanning the potential from – 0.40 V_{SCE}

Table I. Composition of the Super Duplex Stainless Steel (Sandvik SAF-2906™) in Weight Pct Alloying Elements

Elements	C	Si	Mn	P	Cr	Ni	Mo	Cu	N
Weight Pct	0.03	0.3	1.0	0.015	29	7	2.3	0.80	0.35

and stopped before the onset of transpassive region. For further details on the potentiodynamic polarization and analysis, the reader may refer elsewhere.^[37]

III. PHASE-SPECIFIC ELECTROCHEMISTRY

A. Phase-Specific Electrochemical Dissolution and Potentiodynamic Polarization on Single-Phase Working Electrodes

To measure the effect of solution annealing on individual phases (ferrite and austenite), single-phase working electrodes were prepared by selective dissolution of the other phase.^[38–46] To establish the peak potentials (necessary to dissolve each phase), electrochemical polarizations were carried out in deaerated 2 M H₂SO₄ + 0.5 M HCl solution, and the tests were performed at a potential range from – 0.40 to – 0.20 V_{SCE} and at a scanning rate of 20 mV/min. Otherwise, the procedure used was same as the earlier Section II–C. The specimens were held, for 15 hours, at the measured^[38–46] peak potentials for each phase. A 3-D non-contact optical profiler (Zeta™) was used to measure the depth of dissolution of the respective phases. A total 60 line-scans, of each 500 μm in length, were acquired for measuring the average depth of dissolution.

Post-dissolution cavities were filled with a very slow setting epoxy resin. The specimens were then cured for 12 hour. After curing, the extra resin was carefully removed by grinding with fine SiC paper (2500 grit size). Selective dissolution of the ferrite phase, for example, resulted in the formation of cavities by dissolution of the ferrite. This left the austenite phase unaffected. By grinding away the extra epoxy resin, only the austenite phase was exposed. Single-phase ferrite and austenite electrodes were thus prepared. These single-phase electrodes were then subjected to potentiodynamic polarization tests in 1 M H₂SO₄ solution, using a methodology described in Section II–C. Only addition was SEM imaging, to confirm absence of crevice formation at the metal–resin interface.

B. Electrochemical Impedance Spectroscopy (EIS) and Mott–Schottky (M–S) Analysis of Single-Phase Working Electrodes

The single-phase electrodes were also subjected to electrochemical impedance spectroscopy (EIS) and subsequent Mott–Schottky (M–S) analysis. These were needed to establish electronic properties of the respective passive films. A passive potential of 0.2 V_{SCE}, a potential clearly in the passive potential regime: as

obtained from potentiodynamic polarization of single phases, was applied for 10 hours in 1 M H₂SO₄ solution. EIS measurements were performed on this passivated specimen by applying a sinusoidal potential of 10 mV amplitude (with the frequency range of 10 KHz to 10 mHz in the potential range of 0.2 to 0.8 V_{SCE} with a step size of 50 mV). The M–S analysis was performed at a fixed frequency of 1000 mHz.^[41,42,48,49] Mott–Schottky relationship determined^[42,50–52] the charge distribution at the semiconductor-solution interface. This was obtained from the electrode capacitance (C) as a function of electrode potential (E), as per Eqs. [1] and [2].

$$\frac{1}{C^2} = \frac{2}{\epsilon\epsilon_0 e N_D} \left(E - E_{fb} - \frac{kT}{e} \right) \quad [1]$$

$$\frac{1}{C^2} = \frac{2}{\epsilon\epsilon_0 e N_A} \left(E - E_{fb} - \frac{kT}{e} \right) \quad [2]$$

where ϵ denotes the dielectric constant of the passive film, ϵ_0 the permittivity of vacuum (8.854×10^{-12} F/m), e represents electron charge, N_D denotes the donor density for n-type semiconductor and N_A denotes the acceptor density for p-type semiconductor, E_{fb} is the flat band potential, k is the Boltzmann constant and T is the absolute temperature.

C. Fourier-Transformed Infrared (FTIR) Imaging

For the FTIR-imaging, a Bruker™ 300-Hyperion unit was used. It is to be noted that the approximate FTIR wavenumber of the Cr₂O₃ film is 660 cm⁻¹.^[53–55] Past studies^[53] had used EBSD plus FTIR-imaging as an effective means for relating substrate microstructure with stability or retention of the Cr₂O₃ film. The same methodology was adopted, in the present study, for the single-phase electrode specimens. While EBSD provided the substrate microstructure, post-anodic polarization Cr₂O₃ films were characterized as area under the Cr₂O₃ peak.

D. Thermo-Kinetic Simulations

Thermo-kinetic simulations were also carried out to predict ‘limited’ austenite-to-ferrite phase transformations and evolution of phase-specific chemistry. Dictra™, a module associated with Thermo-Calc™ software, was employed. This module enabled calculation of kinetics of phase transformations of a multi-component alloy.^[56–58] The module included appropriate database of both thermodynamic parameters and concentration plus temperature-dependent

diffusion coefficients. ‘Moving phase boundary’ model, interface migration being controlled by the mass balance, was employed. It is to be noted that the model involved the flux of elements diffusing across the interface and the establishment of local equilibrium at the interface: a combination of MOBFE4 database of Dictra™ plus TCFE9 database of Thermo-Calc™. The nucleation was not considered. Further, silicon concentration was also not considered: the effective silicon content was added to the chromium concentration.

IV. RESULTS

Figure 1(a) shows EBSD images of the same region before and after the solution annealing (1323 K, 8 hour). Appropriate circles and arrowheads are used, in the figure, to indicate direct evidences of grain coarsening and austenite-to-ferrite phase transformation. Data from multiple EBSD scans (of direct microstructural observations) were then collated to present a consolidated picture of the solution annealing-induced microstructural evolution: coarsening of the austenite

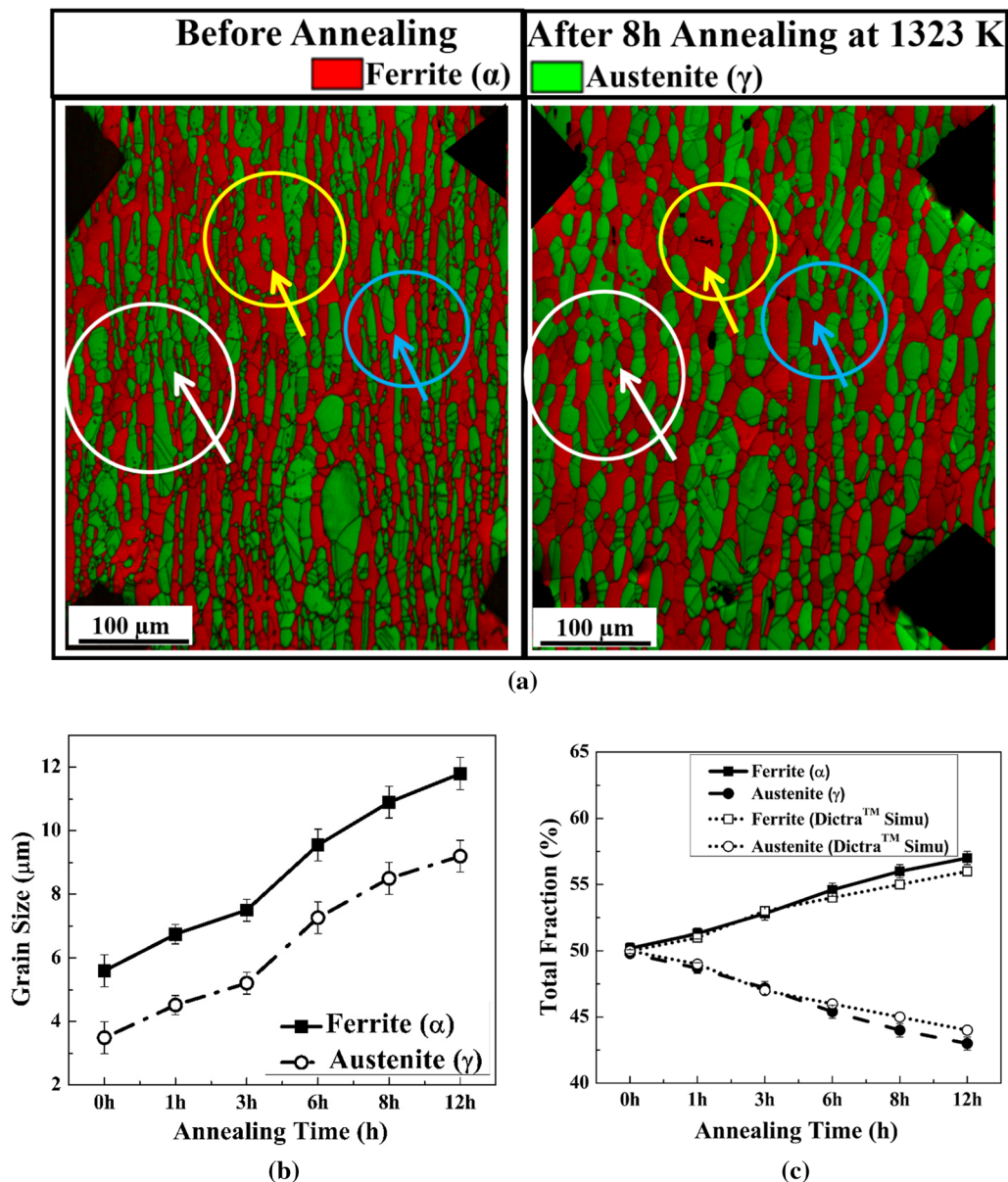


Fig. 1—Direct observations, with EBSD (electron backscattered diffraction), on annealing induced coarsening and austenite-to-ferrite transformation. (a) This is shown, with image quality (IQ) plus phase maps, on specimens before and after 1323 K (1050 °C) annealing for 8 h. Data from different annealing time periods were then collated to show (b) grain size and (c) phase fraction vs annealing time. In (a) circles plus arrow heads are used to indicate both grain coarsening and austenite-to-ferrite transformation, while (c) also reports Dictra™ simulations. Error bars in (b) and (c) represent standard deviations from multiple EBSD scans.

and ferrite grains (see Figure 1(b)) and changes in phase fractions (Figure 1(c)). The grain size was estimated from the standard linear intercept, using boundaries with misorientation > 5 deg. In the starting as-received structure (0 hour annealing), the ferrite grains were marginally coarser than the austenite grains (5 vs 3 μm). The size advantage of the ferrite grains continued throughout the solution annealing, evolving into respective average grain sizes of 12 and 9 μm (for the ferrite and the austenite phases, respectively) after 12 hours of annealing (Figure 1(b)). The grain coarsening was accompanied by changes in ferrite and austenite phase content: or ‘limited’ (~ 7 pct by area) austenite-to-ferrite phase transformation (see Figure 1(c)). More specifically, austenite volume fraction dropped monotonically from ~ 50 to ~ 43 pct. Naturally, this was accompanied by a corresponding increase in the ferrite fraction. The DictraTM captured the quantitative patterns of this austenite-to-ferrite phase transformation very effectively.

The grain coarsening reduced the relative presence of the austenite–ferrite interface: the interface length per unit area dropped monotonically with annealing time, see Figure 2(a). Further, it is to be noted that austenite–ferrite boundary had a preferred boundary nature. As shown in the misorientation distribution function (MDF)^[59–61] section in Figure 2(b), there was a clear bias for 45 deg $\langle 001 \rangle$ axis-angle boundary misorientation. However, this boundary nature as represented by boundary number fraction vs deviation from 45 deg $\langle 001 \rangle$, did not appear to change with annealing time. In summary, solution annealing induced microtextural changes were clearly identified as grain coarsening plus ‘limited’ (~ 7 pct) austenite-to-ferrite phase transformation. However, there was no evidence of the change in the interface nature with annealing duration.

Changes in the phase-specific chemistry constituted another important observation. As shown in Figure 3, SEM-WDS peak profiles were measured for different elements: for example, molybdenum in austenite and ferrite (see Figure 3(a)). Nitrogen quantification was avoided due to its lower atomic number (and correspondingly large background). From WDS peak profiles (Figure 3(a)), and using appropriate standards,^[62] the phase-specific elemental compositions were measured at different stages of solution annealing. The experimental (WDS measurement) as well as the simulated (DictraTM) compositions showed a similar trend. Such trends can be described as monotonic drop and increase of Cr in ferrite (Figure 3(b)) and austenite (Figure 3(c)). Exactly opposite trend was observed for Ni (see Figures 3(d) and (e)). The Mo in ferrite (Figure 3(f)) also dropped monotonically, while in austenite a non-monotonic behavior was observed (Figure 3(g)). It is important to note that these experimental trends were captured effectively by the DictraTM simulations.

DictraTM simulations provided explanations for the observed experimental composition changes. This explanation is largely based on the chemical potential gradients, as a function of solution annealing time, across the ferrite and the austenite phases. The increase in annealing time enabled decreased presence of Cr

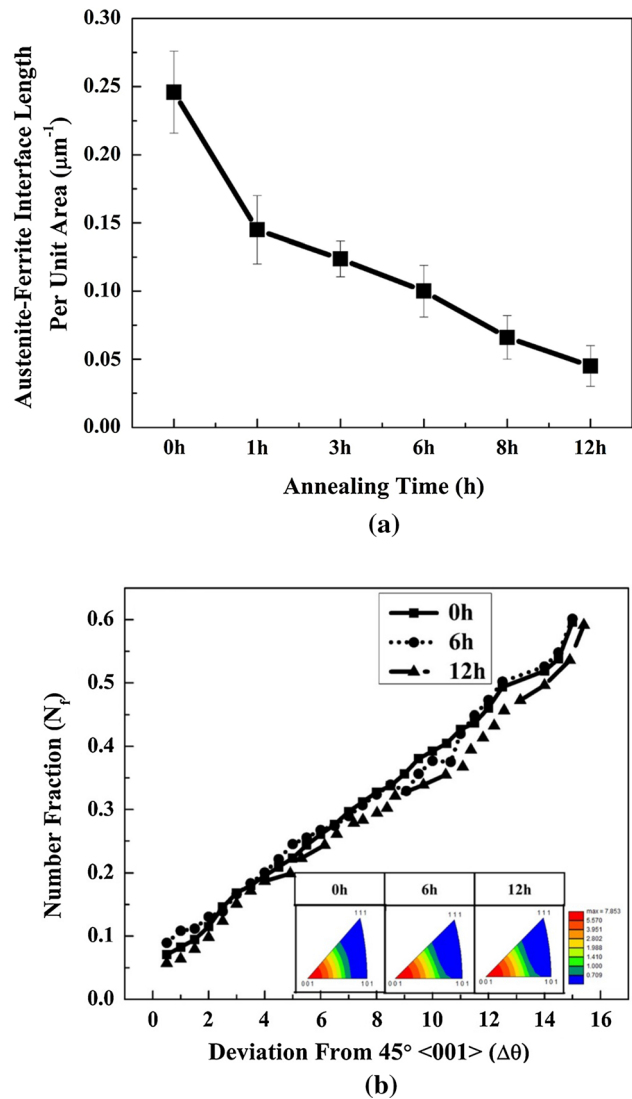


Fig. 2—Coarsening induced changes in the austenite–ferrite interface. (a) Austenite–ferrite interface length per unit area vs annealing time. (b) Number fraction of austenite–ferrite boundaries at different deviations from 45 deg $\langle 001 \rangle$. This is shown for three different annealing periods. Also included are the appropriate MDF (misorientation distribution function) 45 deg sections for these annealing periods.

(Figure 3(b)) & Mo (Figure 3(f)) in ferrite and Ni (Figure 3(e)) in austenite. Being respective phase stabilizers, Mo and Cr partitioned towards ferrite, while Ni and N did the same for austenite.^[1,63–68] DictraTM showed increased chemical potential gradients for Mo and Cr in the austenite. This was mainly due to the diffusion of nitrogen from austenite-to-ferrite. The diffusion of nitrogen (from austenite-to-ferrite) and diffusion of Cr and Mo (from ferrite to austenite) increased and decreased the Cr and Mo concentrations in austenite (Figure 3(c)) and ferrite (Figures 3(b) and (f)) phases, respectively. Beyond a certain annealing time (3 to 6 hour), nitrogen content in the ferrite reached saturation (as calculated by DictraTM). This led to chemical potential of nitrogen in the ferrite to increase, and allowed diffusion of nitrogen from ferrite to

austenite. This diffusion of nitrogen, and the fact that Mo diffusion in the austenite is very slow,^[63–65] affected the Mo concentration. The Mo content increased (in the

austenite phase) marginally till 6 hours of annealing and then dropped with annealing beyond 6 hours. As presented later in the manuscript, the electrochemical

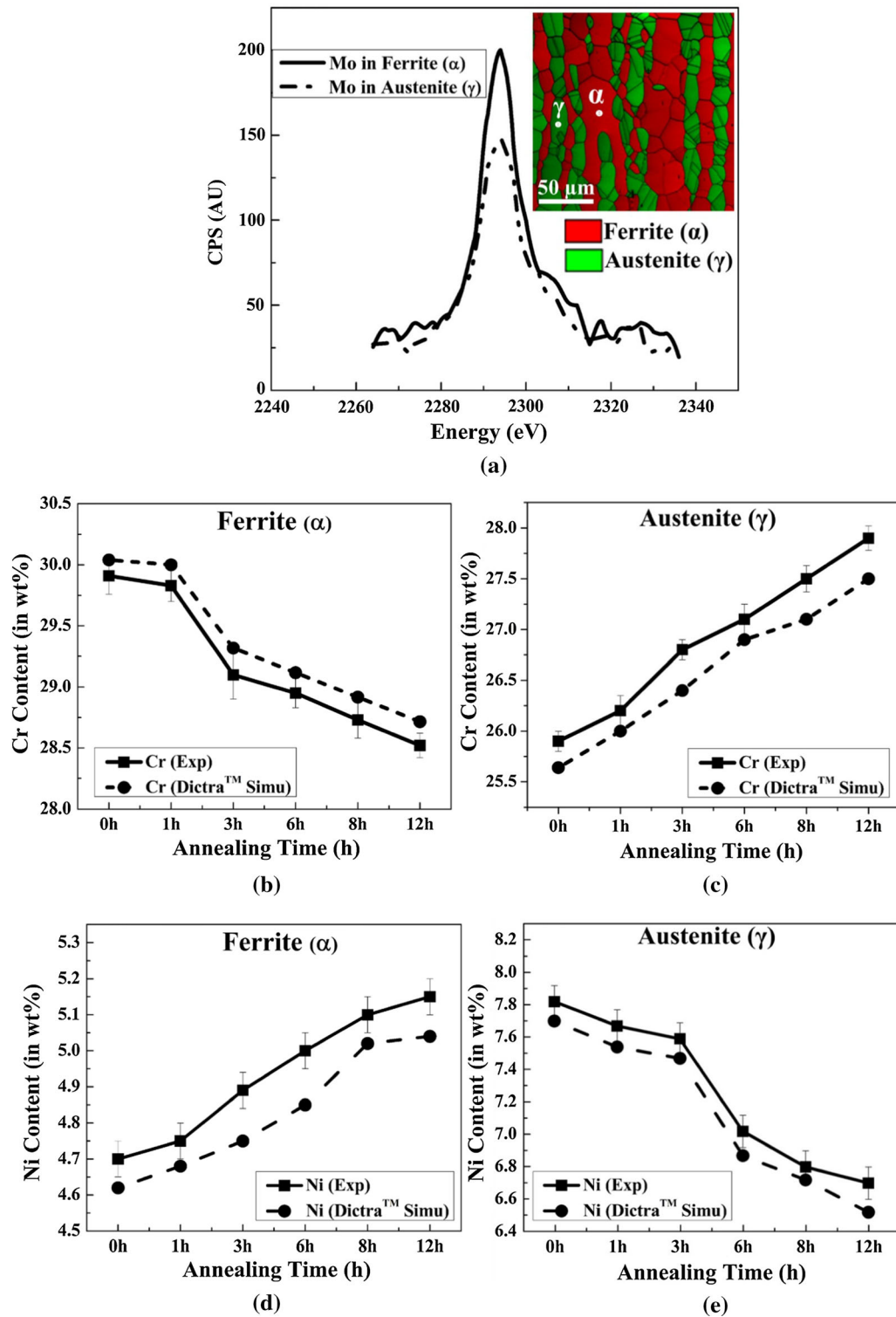


Fig. 3—(a) EBSD microstructure (0 h annealing) with WDS (wave length-dispersive X-ray spectroscopy) ‘point’ measurements. Included are WDS peaks (counts per seconds, CPS, vs energy) for molybdenum (Mo) in austenite and ferrite. WDS estimated elemental (Cr, Ni and Mo) compositions in ferrite (b), (d), (f) and in austenite (c), (e), (g) vs annealing time. At least 20 ‘points’ were measured to provide the average and the standard deviations (shown as error bars). (b) to (f) also provide simulated chemical compositions from DictraTM.

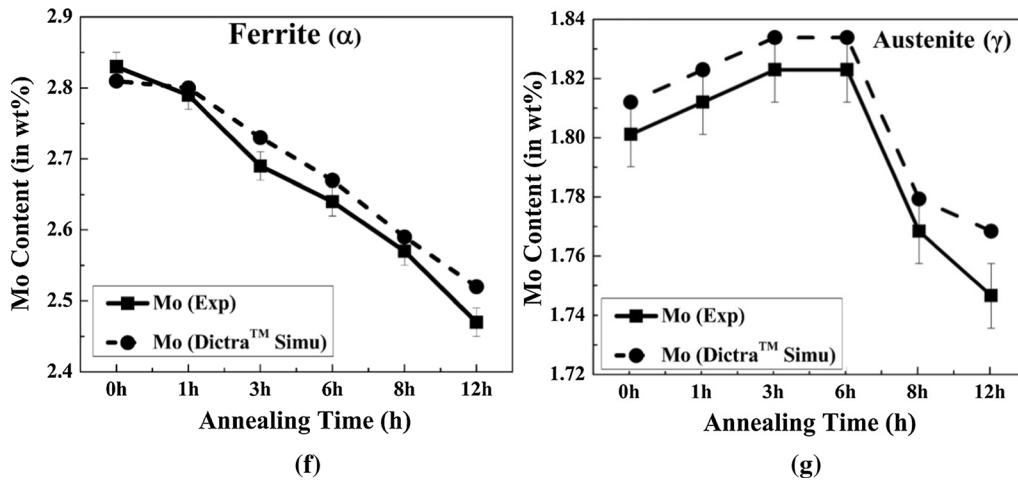


Fig. 3—continued.

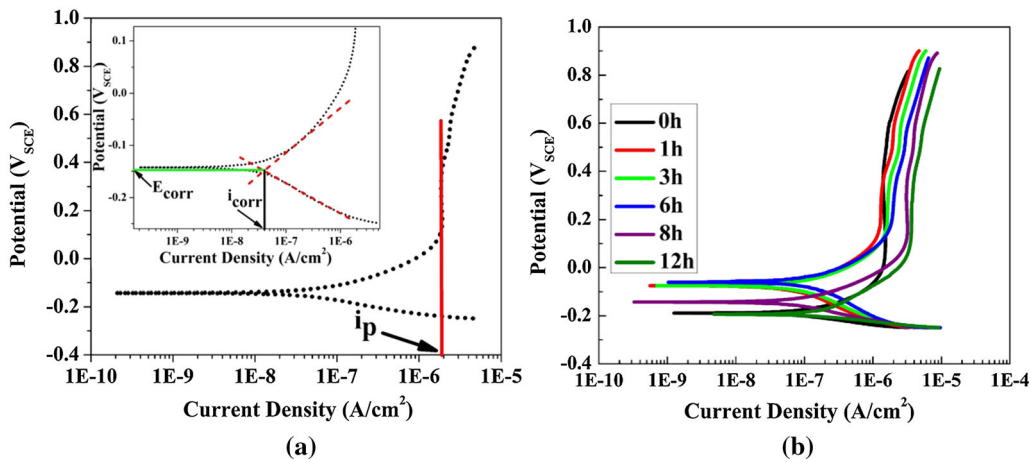


Fig. 4—(a) Standard Tafel analysis^[69,70] of anodic polarization data. Intersection of anodic and cathodic Tafel lines provides corrosion current (i_{corr}), corresponding potential being E_{corr} . Passive region, where current does not get strongly affected by change in potential, of the anodic plot gives passivation current (i_p). (b) Potentiodynamic polarization with 1 M H_2SO_4 .

behavior of the austenite phase was largely determined by grain coarsening plus non-monotonic changes in the Mo concentration.

All such microstructural changes are naturally expected to reflect on the electrochemical behavior.^[8,10,11,16–24,26–35] The anodic polarization data are interpreted with Tafel analysis.^[69,70] This is shown in Figure 4(a). As shown in the figure (and described in the figure caption and elsewhere^[69,70]), the corrosion performance can be captured with corrosion current (i_{corr}), corrosion potential (E_{corr}), and passivation current (i_p). More specifically, drop in i_{corr} or i_p indicate enhanced passivation (or resistance to corrosion), while an increase represent degradation.^[37] As indicated in Figure 4(b) and summarized in Table II, there was a clear degradation after 8 and 12 hour solution annealing. The general corrosion behavior (with the composite two-phase electrode), however, did not capture possible changes associated with shorter annealing durations. It was hence decided to expand the electrochemistry to (i)

dissolution of individual phase and (ii) polarization behavior with single-phase electrodes.

As shown in Figures 5(a) and (b), and described in further details elsewhere,^[38–46] appropriate anodic polarizations tests (in 2 M H_2SO_4 + 0.5 M HCl) identified the dissolution peak potentials for the ferrite (α) and the austenite (γ) phases. It is to be noted, from Figures 6(a) and (b), that at all stages of solution annealing the α (the phase easier to dissolve) had higher dissolution current density than γ . By applying appropriate peak dissolution potentials (see Figure 5), the specific phases were selectively dissolved. As described in the experimental procedure, this was achieved by appropriate electrochemical potentiostatic exposures in 2 M H_2SO_4 + 0.5 M HCl solution for 15 hours. The measured depth of dissolution (as measured by 3d profilometer) with annealing time showed clear differences (Figure 6(c)). For ferrite phase, depth of dissolution increased monotonically with solution annealing time. The austenite phase, however, showed a clear

Table II. The i_p , i_{corr} (in $\mu\text{A}/\text{cm}^2$) and E_{corr} (mV_{SCE}) of 2906 Super Duplex Stainless Steel (Figure 4(a)) at 1323 K (1050 °C) for Different Annealing Time in 1M H_2SO_4 Solution

Annealing Time	0 h	1 h	3 h	6 h	8 h	12 h
i_p ($\mu\text{A}/\text{cm}^2$)	1.48	1.29	1.62	1.90	3.17	3.67
i_{corr} ($\mu\text{A}/\text{cm}^2$)	0.084	0.078	0.072	0.07	0.1	0.17
E_{corr} (mV_{SCE})	- 188	- 80	- 75	- 62	- 156	- 197

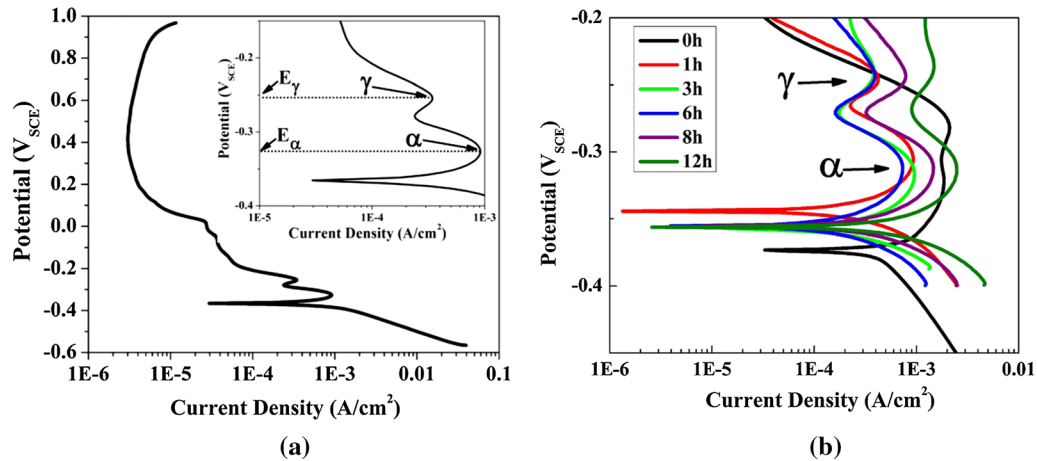


Fig. 5—(a) Potentiodynamic polarization with 2 M H_2SO_4 + 0.5M HCl showing clear ferrite (α) and austenite (γ) dissolution peaks and corresponding potentials. (b) Similar potentiodynamic polarization plots for specimens subjected to different solution annealing (1323 K (1050 °C)) durations.

non-monotonic behavior: lowering of dissolution depth till 6 hour, followed by an increase. Much of the subsequent manuscript is devoted to explore this non-monotonic corrosion performance of the solution-annealed austenite phase.

The selective dissolution of the phases was followed by preparation of single-phase electrodes. As shown in Figure 7(a), the dissolved “ditches” of the ‘other’ phase were carefully filled with a non-conducting resin. The single-phase electrode was then subjected to anodic polarization tests separately for the ferrite (Figure 7(b)) and the austenite (Figure 7(c)) phases. Further, phase-specific passivation current density (i_p), corresponding to passive potential of $0.2 V_{\text{SCE}}$ (i_p : Figure 7(d)), and corrosion current density (i_{corr} : Figure 7(e)) were estimated from the appropriate single-phase potentiodynamic polarizations plots (Figures 7(a) and (b)). All the experiments were repeated thrice to confirm the reproducibility. The i_p and i_{corr} showed an identical pattern as that of phase-specific depth of dissolution (Figure 6(c)). In a word, local dissolution (Figure 6(c)) and single-phase electrochemistry (Figures 7(d) and (e)) showed identical trends of monotonic increase, with annealing time, in ferrite and a clear non-monotonic pattern for the austenite phase.

The dissolution and electrochemistry of the respective phases are expected^[41–44] to depend on the electronic property, or donor–acceptor densities, of the corresponding oxides. It is to be noted that the passive films are categorized^[14,52] as p-type and n-type oxides.

Their electronic properties naturally affect the electron transfer reactions, and the film stability.^[14] For example, the n-type passive film is expected^[14,52,71,72] to be more stable, electrochemically, than the p-type. Oxide film electronic properties can be obtained^[41,42,44,73,74] by Mott–Schottky (M–S) analysis (Eqs. [1] and [2]). The M–S plots for both the phases (Figures 8(a) and (b)) showed positive slopes. This indicates^[14,52] n-type semiconductor nature of the passive film(s). Figure 8(c), on the other hand, shows the calculated defect density (N_D) values of the respective passive films in the ferrite and the austenite phases. It is to be noted that the N_D values represent cation-vacancy density in the passive film, which arises from the dissolution of cations at the film–solution interface. For a better chemical stability of the passive film and a lower diffusion, a lower value of the N_D is desired.^[41,42,44,50–52,71,73,74] The plot of defect density with increasing annealing duration for ferrite showed a monotonic increase in defect density (Figure 8(c)) in the ferrite phase. Austenite, on the other hand, showed a non-monotonic behavior (Figure 8(c)).

It is apparent that the ferrite phase had monotonic pattern of grain coarsening (Figure 1(b)) and decrease in Cr (Figure 3(b)) and Mo (Figure 3(f)) contents (Figure 3(b)). The ferrite phase also had a monotonic drop in corrosion resistance (Figures 6(c), 7(d), (e) and 8(c)). The electrochemistry of the austenite phase was, however, clearly non-monotonic. The austenite phase also had monotonic grain coarsening (Figure 1(b)), but

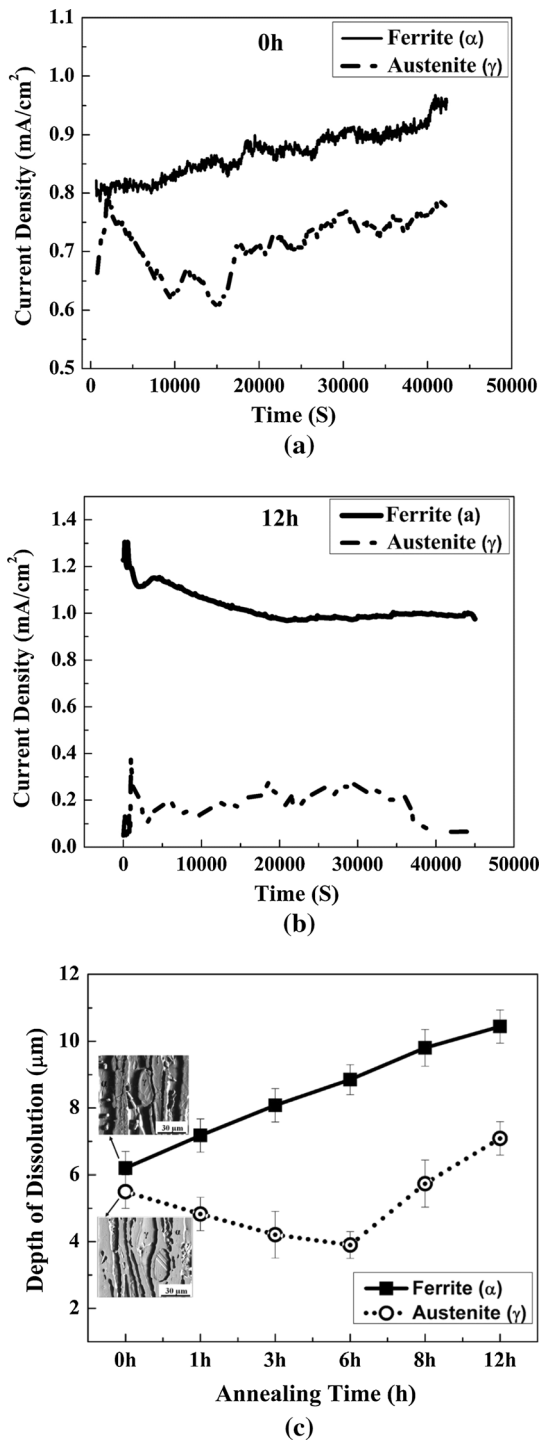


Fig. 6—Current density vs time for specimens with (a) 0 h and (b) 12 h solution annealing. Austenite current density was lower than ferrite in (a), and the difference was even more in (b). (c) Depth of dissolution, as measured by non-contact profilometer: Zeta™, vs annealing time for austenite and ferrite.

a non-monotonic evolution in Mo content (Figure 3(g)). Was the corrosion performance of the austenite phase determined by a balance between grain size and Mo content? To explore this point, a combination of FTIR-imaging plus EBSD was used.

A previous study,^[53] albeit on austenitic stainless steel, successfully related substrate microstructure with FTIR Cr-oxide (Cr₂O₃) peak. It was shown^[53,55] that the area under the peak provided a measure of the stability or retention of the protective oxide film, and hence related with measurements of local corrosion resistance. This present manuscript used the same technique. At least 30 measurements, in each phase and annealing time periods, showed a steady drop in the area under Cr₂O₃ peak for the ferrite phase (Figure 9(a)). For the austenite phase, on the other hand, a non-monotonic pattern was clearly noted. It is clear that coarser grain size adversely affected Cr₂O₃ peaks both in ferrite (Figure 9(b)) and in austenite (Figure 9(c)). The data on austenite were further coupled with WDS measurements on Mo content, and then binned for different grain sizes (Figure 10). The collated data, clearly shows that the Cr₂O₃ peak diminished with (i) increase in grain size and (ii) drop in Mo content. It is hence established, phenomenologically, that the corrosion performance of the austenite phase, in SAF-2906™, during solution annealing was determined by a balance between the grain size and the Mo content.

V. DISCUSSION

Solution annealing is associated with routine industrial production, and post-weld heat treatments, in both austenitic stainless steels^[75,76] and austenite-ferrite duplex stainless steels.^[1,2,4] In DSS, the solution annealing temperature is grade specific.^[1,2,4,6] In lean DSS, for example, a temperature of ~ 1273 K (1000 °C) is used.^[1] The standard and super DSS grades, on the other hand, require ~ 1323 K to 1343 K (1050 °C to 1070 °C) for solution annealing: which is extended to as high as ~1373 K (1100 °C) for tungsten-bearing grades.^[1,4] The selection of solution annealing temperatures, in DSS, appears to originate from three factors: (i) ability to dissolve unwanted intermetallic phases, (ii) to obtain appropriate phase-mix and (iii) to provide relative homogenization of the chemical composition. Naturally, different aspects of solution annealing temperature induced microstructure-property are not uncommon in the domain of the published literature.^[8–11] Interestingly, however, no such publication is available (to the best possible knowledge of the present authors) on the possible role of solution annealing duration. And this was the starting point of the present study.

Solution annealing is expected to enforce^[16–20] changes in phase-specific chemical composition. The solution annealing temperature is estimated to decrease the PREN of ferrite and increase the PREN of austenite.^[16–20,77,78] A combination of these two has often been argued^[8,19] to non-monotonically affect the critical pitting temperature or CPT. The CPT is measured from cyclic anodic polarization in a chloride solution. However, such CPT measurement cannot be made phase-specific and may offer large measurement uncertainty. Use of single-phase working electrodes (Figures 6(c), 7 and 8) plus FTIR-imaging (Figures 9 and 10) resolved such difficulties. This study successfully

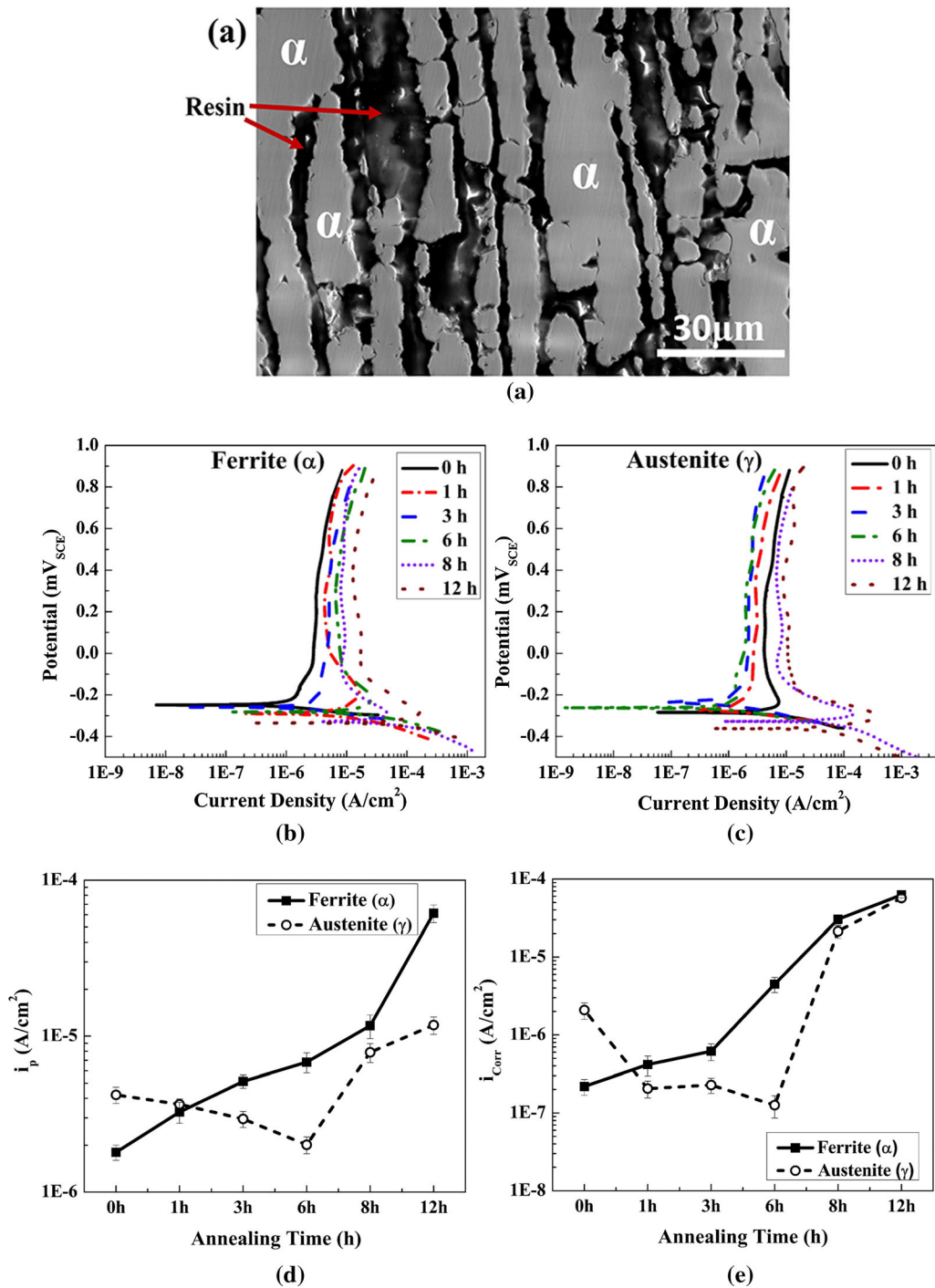
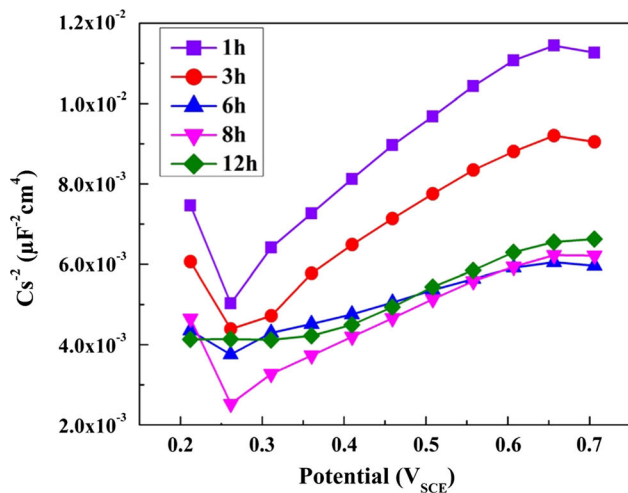


Fig. 7—Post-dissolution specimen, as in Fig. 6(c), were filled with resin and single-phase, austenite or ferrite, electrodes were prepared. (a) SEM (scanning electron microscopy) image of a single-phase ferrite electrode. Polarization curves (in 1M H₂SO₄) of (b) ferrite and (c) austenite single-phase electrodes for different annealing periods. From such polarization curves, (d) i_p (passivation current) and (e) i_{corr} (corrosion current) values were calculated and plotted as a function of annealing time.

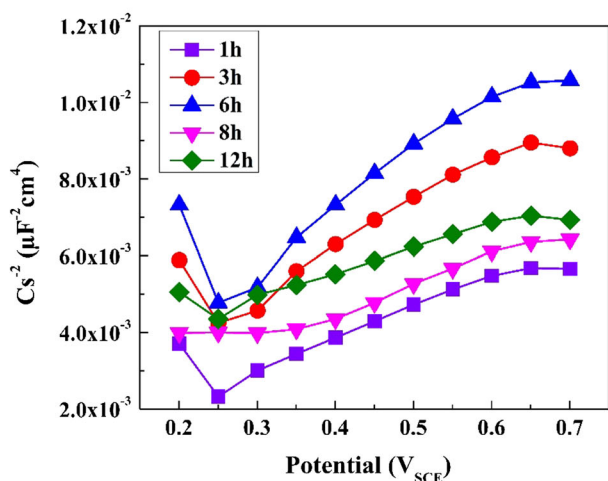
related microstructural parameters, grain size and phase-specific chemistry, with resistance to uniform and local corrosion.

A reader may question the extensive use of phase-specific electrochemistry, a critical niche, in this study: especially as the two-phase corrosion performance is often governed^[79] by galvanic coupling. The

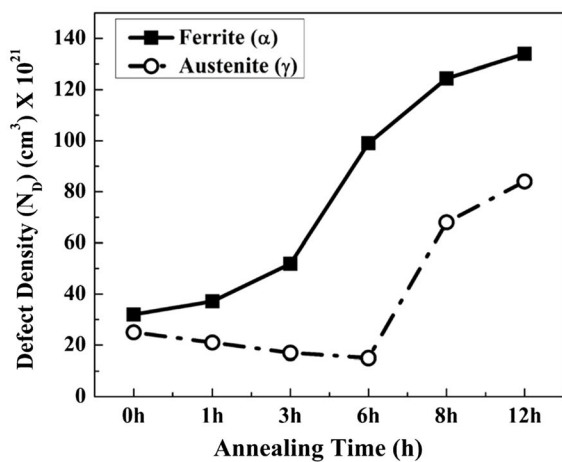
latter is known^[79,80] to depend on: (i) electrochemical environment, (ii) area fraction of the phases and (iii) potential difference (OCP—see Table III) between the phases. (iii) is expected to depend on the nature of the phase boundary, which did not change noticeably (Figure 2) in the present study. More importantly, the potential difference (Table III) did not differ



(a)



(b)



(c)

Fig. 8—Mott-Schottky (M-S) plots, in 1M H₂SO₄ solution, from single-phase electrodes of (a) ferrite and (b) austenite. These are shown for different annealing time periods. (c) The effect of annealing time on defect density: as estimated from M-S analysis.

significantly, between the two phases, with annealing time. In other words, it can be safely stated that the galvanic coupling between the phases was not the critical parameter determining the resistance to corrosion: and Tafel analysis of the general corrosion (or two-phase working electrode) does not provide a clear picture of the corrosion performance. This manuscript hence extensively used single-phase working electrodes for electrochemical characterization (Figures 7 and 8). It is to be noted that this method is non-trivial (takes about 4 to 5 working days for a single measurement), and had rarely,^[37–44] been used for relating microstructure with corrosion performance in DSS. This, and the direct experimental observations on annealing induced microstructural evolution, provided two very interesting features of the present experimental study.

Finally, electrochemistry of the single-phase working electrode was used in conjunction with FTIR-imaging (Figures 8 and 9). And they provided a unique perspective on phase-specific corrosion performance with solution annealing induced microstructural evolution. Corrosion resistance of the ferrite phase dropped monotonically with annealing time (Figures 7(d) and (e)): a result of measured drop in Cr (Figure 3(b)) and Mo (Figure 3(f)) contents and increase in grain size (Figure 1(b)). For the austenite phase, on the other hand, detrimental aspect of grain coarsening was balanced (at least during initial solution annealing stages) by increase in Mo content. In the subsequent paragraphs, the role of grain size and Mo content, with an emphasis on the electronic property of the protective oxide film, are further deliberated.

Stainless steels, in general,^[24,25,81,82] and DSS, in particular,^[21–23] are known to improve their corrosion performance with grain size refinement. However, experimentally reported grain size range for such improvement differs between the grades. More specifically, corrosion resistance of DSS has been reported^[21–23,25] to improve, noticeably, when grain size reduced from 10 seconds of micron to a few hundred nm. This study, on the other hand, experimentally captured (Figure 9) reduced presence of the Cr₂O₃ film, in both austenite and ferrite phases, even with ‘limited’ (several microns) coarsening of grains. Three different models have been proposed to explain the beneficial aspects of grain size refinement: (i) conversion of Cr(OH)₃ to Cr₂O₃,^[21–25] (ii) higher boundary density promoting Cr diffusion (bulk to surface) and formation of Cr₂O₃ film,^[21–25,81,82] and (iii) lower defect density enhancing film stability.^[21–25,81,82] While the present manuscript did not provide direct experimental evidence in support of the first two models, the Mott-Schottky analysis of the oxide film (Figure 8(c)) indicated time-dependent evolution of donor-acceptor densities. More specifically, the film defect densities (Figure 8(c)) scaled with the corrosion performance of single-phase working electrodes (Figures 7(d) and (e)).

To appreciate Figure 8(c) (and its relation with Figures 7(d) and (e)) better, a deliberation on the

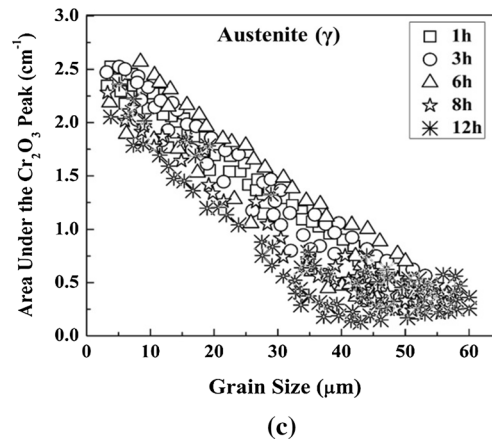
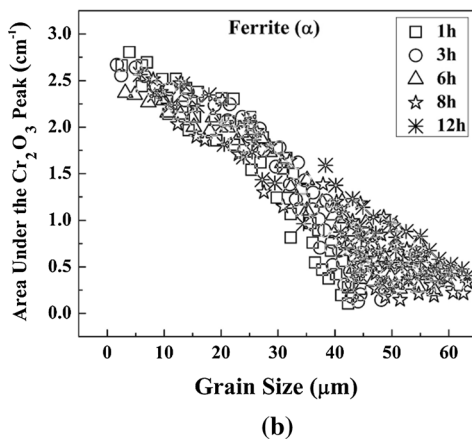
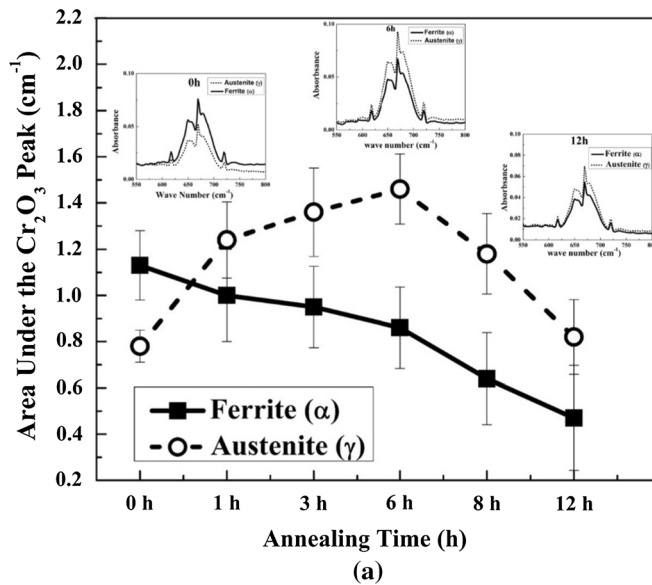


Fig. 9—(a) Average area under the Cr_2O_3 peaks, for austenite and ferrite phases, at different solution annealing time periods. These were estimated from site-specific FTIR (Fourier-transformed infrared spectroscopy) imaging spectra—shown for 0, 6 and 12 h annealing. Area under the Cr_2O_3 peaks for different (b) ferrite and (c) austenite grain-sizes and for different time periods.

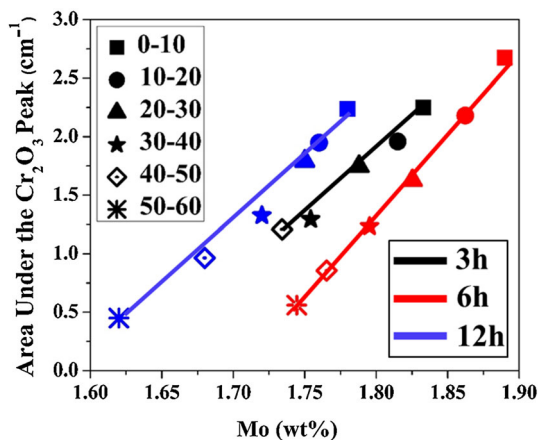


Fig. 10—Area under Cr_2O_3 peaks vs molybdenum (Mo) concentration. The data were plotted using different grain size binning and different annealing time periods.

semiconductor nature of the oxide film is warranted. The protective oxide film of a stainless steel is known to act as a highly doped semiconductor, with a defect density in the range of 10^{20} to 10^{21} cm^{-3} .^[12–14,52] These defects include anion vacancies, cation vacancies and cation interstitials. And the defect density is expected to decide the semiconductor behavior and film stability.^[50,52,71] If cation interstitials and oxygen vacancies dominate then the oxide film is an n-type semiconductor (or primarily an electron donor). For dominant role of cation vacancies, on the other hand, the film becomes an electron acceptor or a p-type semiconducting oxide. The positive slopes of the M–S data (Figures 8(a) and (b)) clearly showed the n-type nature of the DSS oxide films in passive potential regime. It is hence expected the film defect density (Figure 7(c)) to determine the corrosion performance.^[12–14,50,52,71,72] That is exactly what was observed in the ferrite phase: grain coarsening of the ferrite phase increased the defect density and reduced

Table III. The OCP (mV_{SCE}) of Ferrite (α) and Austenite (γ) Phase in 2906 Super Duplex Stainless Steel (Figures 6(b) and (c)) at 1323 K (1050 °C) for Different Annealing Time 1M H₂SO₄ Solution

Annealing Time	0 h	1 h	3 h	6 h	8 h	12 h
Ferrite (α)	– 250	– 290	– 259	– 282	– 328	– 335
Austenite (γ)	– 280	– 272	– 235	– 262	– 327	– 360

the corrosion performance (Figures 6(c) and 7(e)) plus stability or retention (Figure 9(b)) of the oxide film. The austenite phase, on the other hand, showed a non-monotonic behavior: a balance (Figure 10) between grain coarsening and substrate Mo content.

Mo in combination with Cr is reported^[26–35] to be very effective in stabilizing the passive film. More specifically, the polarity of passive film is expected^[31,83] to be modified by the formation of molybdates. Molybdates may convert, through formation of negative MoOⁿ in the outer layer of the film, the intrinsic anionic selectivity behavior to cationic behavior.^[26,29–31,33–35] The resultant bipolar film is expected^[26,29–31,33–35] to facilitate migration of oxide ions: thus, promoting Cr₂O₃ film formation. In addition, Mo may also improve^[23,24] the repassivation by generating MoO₃ or MoO^{2–}. Further, highly stable and insoluble compounds (such as FeMoO₄ and MoO₃) can be promoted^[26,29–31,33–35] by the presence of Mo—enhancing the stability of the passive film. Presence of Mo near the metal–oxide interface may prevent the dissolution rate of iron and chromium.^[84–86]

Though this study did not explore the exact mechanistic origin(s), it clearly related (Figure 10) the Mo presence with stability and retention of the Cr₂O₃ film. It is largely speculative, at this stage, to extend the present observation to other grades of DSS. However, it is apparent that the optimized solution annealing time-temperature is to be based on relative Mo content of the austenite phase (as decided by the phase-specific chemical potentials and diffusivities).

VI. CONCLUSIONS

- Solution annealing (increased time duration up to 12 hour at 1323 K (1050 °C)) induced microstructural changes were quantified as:
 - grain coarsening of both ferrite and austenite phases
 - ‘limited’ (~ 7 pct by area) austenite-to-ferrite phase transformation
 - Changes in phase-specific chemistry: Monotonic increase in Cr and decrease in Ni in austenite; decrease in Cr & Mo and increase in Ni in ferrite. Mo, on the other hand, increased in austenite till 6 hours and then dropped.
- Selective dissolution of individual phases enabled measurements of phase-specific dissolution depths and creation of single-phase working electrodes. The

single-phase electrodes were used to evaluate different aspects of electrochemical performance (i_{corr} and i_p : corrosion and passivation current density respectively and ND: defect density in oxide film). Finally, substrate microstructures were related, with FTIR-imaging, to the stability/retention of the oxide films. It was shown that:

- Corrosion performance (i_p and i_{corr}) of the ferrite phase deteriorated monotonically, with time. This coincided with increase in oxide defect densities and lower stability of the Cr₂O₃ film (area under Cr₂O₃ peak from FTIR)—features attributed to grain coarsening and diminished Cr & Mo presence in ferrite phase with increasing time of solution annealing.
- Corrosion of the austenite phase was, however, non-monotonic. It improved till 6 hours annealing and then degraded. It was shown that increase in substrate Mo concentration counter-balanced the deleterious effects of grain coarsening (at least during the initial 6 hour of solution annealing). Mo content in austenite decreased after 6 hours of solution annealing resulting in lower corrosion performance (i_p and i_{corr}).

ACKNOWLEDGMENTS

The authors would like to acknowledge support from Sandvik Materials Technology, CoEST (center of excellence on steel technology, IIT Bombay). Support from the National Facility of Texture and OIM (IIT Bombay) and SAIF (Sophisticated Analytical Instrumentation Facility) is also appreciated.

REFERENCES

1. R.N. Gunn: *Duplex Stainless Steels: Microstructure, Properties and Applications*, Woodhead Publishing, Sawston, 1997.
2. I.M. Association: *Practical Guidelines for the Fabrication of Duplex Stainless Steel [M/OL]*, The International Molybdenum Association, London, 2009.
3. P. Antony, R.S. Raman, P. Kumar, and R. Raman: *Metall. Mater. Trans. A*, 2008, vol. 39A, pp. 2689–97.
4. J.O. Nilsson: *Mater. Sci. Technol.*, 1992, vol. 8, pp. 685–700.
5. M. Okayasu and D. Ishida: *Metall. Mater. Trans. A*, 2019, vol. 50A, pp. 1380–88.
6. J. Charles: *Steel Res. Int.*, 2008, vol. 79, pp. 455–65.
7. S.K. Ghosh, D. Mahata, R. Roychaudhuri, and R. Mondal: *Bull. Mater. Sci.*, 2012, vol. 35, pp. 839–46.
8. B. Deng, Y.M. Jiang, J. Gao, and J. Li: *J. Alloys Compds.*, 2010, vol. 493, pp. 461–64.

9. S.C. De Rezende, M.E.R. Cronemberger, R. Silva, C.A.D. Rovere, S.E. Kuri, L.L. de Sousa, N.A. Mariano: *Materials Science Forum*, Trans Tech Publ, 2018, vol. 930, pp 374–79.
10. Z. Cvijović and G. Radenković: *Corros. Sci.*, 2006, vol. 48, pp. 3887–3906.
11. M. Gholami, M. Hoseinpoor, and M.H. Moayed: *Corros. Sci.*, 2015, vol. 94, pp. 156–64.
12. J.J. Kim and Y.M. Young: *Int. J. Electrochem. Sci.*, 2013, vol. 8, pp. 11847–59.
13. M.H. Dean and U. Stimming: *Corros. Sci.*, 1989, vol. 29, pp. 199–211.
14. N. Sato: *J. Electrochem. Soc.*, 1982, vol. 129, pp. 255–60.
15. J.O. Nilsson, P. Kangas, A. Wilson, and T. Karlsson: *Metall. Mater. Trans. A*, 2000, vol. 31A, pp. 35–45.
16. P.O. Malta, B.L. Condé, R.F. Assumpção, D.B. Perasoli, D.C. Sicupira, and D.B. Santos: *Metall. Mater. Trans. A*, 2019, vol. 6A, pp. 2665–77.
17. M. Naghizadeh and M.H. Moayed: *Corros. Sci.*, 2015, vol. 94, pp. 179–89.
18. L. Zhang, W. Zhang, Y. Jiang, B. Deng, D. Sun, and J. Li: *Electrochim. Acta.*, 2009, vol. 54, pp. 5387–92.
19. H. Tan, Z. Wang, Y. Jiang, D. Han, J. Hong, L. Chen, L. Jiang, and J. Li: *Corros. Sci.*, 2011, vol. 53, pp. 2191–2200.
20. S.H. Jeon, S.T. Kim, S.Y. Kim, M. S. Choi, Y.S. Park: *Mater. Trans.*, 2013, pp. M2012402.
21. J. Lv, T. Liang, C. Wang, and L. Dong: *J. Electroanal. Chem.*, 2015, vol. 757, pp. 263–69.
22. L. Jinlong, L. Tongxiang, W. Chen, and D. Limin: *Mater. Sci. Eng. C*, 2016, vol. 62, pp. 558–63.
23. H. Sarlak, M. Atapour, M. Esmailzadeh, and D. Limin: *Mater. Des.*, 2015, vol. 66, pp. 209–16.
24. K. Ralston and N. Birbilis: *Corrosion*, 2010, vol. 66, pp. 075005–013.
25. J. Lv and H. Luo: *J. Nucl. Mater.*, 2014, vol. 452, pp. 469–73.
26. C.O.A. Olsson: *Corros. Sci.*, 1995, vol. 37, pp. 467–79.
27. I. Olefjord, B. Brox, and U. Jelvestam: *J. Electrochem. Soc.*, 1985, vol. 132, pp. 2854–61.
28. L. Wegrelius and F. Falkenberg: *J. Electrochem. Soc.*, 1999, vol. 146, pp. 1397–1406.
29. M. Ameer, A. Fekry, and F.E.T. Heakal: *Electrochim. Acta*, 2004, vol. 50, pp. 43–49.
30. H.Y. Ha, T.H. Lee, J.H. Bae, and D. Chun: *Metals*, 2018, vol. 8, p. 653.
31. G. Ilevbare and G. Burstein: *Corros. Sci.*, 2001, vol. 43, pp. 485–513.
32. A. Pardo, M. Merino, A. Coy, F. Viejo, R. Arrabal, and E. Matykina: *Corros. Sci.*, 2008, vol. 50, pp. 1796–1806.
33. L. Jinlong, W. Zhuqing, L. Tongxiang, S. Ken, and M. Hideo: *Results Phys.*, 2017, vol. 7, pp. 3459–64.
34. T. Mesquita, E. Chauveau, M. Mantel, N. Kinsman, V. Roche, and R. Nogueira: *Mater. Chem. Phys.*, 2012, vol. 132, pp. 967–72.
35. H. Tian, X. Cheng, Y. Wang, C. Dong, and X. Li: *Electrochim. Acta*, 2018, vol. 267, pp. 255–68.
36. H. Ogawa, H. Omata, I. Itoh, and H. Okada: *Corrosion*, 1978, vol. 34, pp. 52–60.
37. ASTM Standards G5-14^{e1}, *Standard Reference Test Method for Making Potentiodynamic Anodic Polarization Measurements*, 2018, pp. 01–09.
38. W.T. Tsai and J.R. Chen: *Corros. Sci.*, 2007, vol. 49, pp. 3659–68.
39. R. Mondal, S.K. Bonagani, A. Lodh, T. Sharma, P.V. Sivaprasad, G. Chai, V. Kain, and I. Samajdar: *Corrosion*, 2019, vol. 75, pp. 1315–26.
40. A. Bautista, S. Alvarez, and F. Velasco: *Mater. Corros.*, 2015, vol. 66, pp. 347–56.
41. T. Bellezze, G. Giuliani, A. Viceré, and G. Roventi: *Corros. Sci.*, 2018, vol. 130, pp. 12–21.
42. X. Cheng, Y. Wang, C. Dong, and X. Li: *Corros. Sci.*, 2018, vol. 134, pp. 122–30.
43. H. Hwang, G. Lee, S. Jeon, and Y. Park: *Mater. Trans.*, 2009, vol. 50, pp. 1214–18.
44. J.S. Lee, K. Fushimi, T. Nakanishi, Y. Hasegawa, and Y.S. Park: *Corros. Sci.*, 2014, vol. 89, pp. 111–17.
45. I.H. Lo, Y. Fu, C.J. Lin, and W.T. Tsai: *Corros. Sci.*, 2006, vol. 48, pp. 696–708.
46. X. Cheng, Y. Wang, X. Li, C. Dong: *J. Mater. Sci. Technol.*, 2018.
47. M.E. Orazem and B. Tribollet: *Electrochemical Impedance Spectroscopy*, Wiley, New York, 2017.
48. H. Luo, C. Dong, K. Xiao, and X. Li: *Appl. Surf. Sci.*, 2011, vol. 258, pp. 631–39.
49. K. Darowicki, S. Krakowiak, and P. Ślepski: *Electrochim. Acta*, 2006, vol. 51, pp. 2204–08.
50. I. Nicić and D.D. Macdonald: *J. Nucl. Mater.*, 2008, vol. 379, pp. 54–58.
51. R. Jiang, C. Chen, and S. Zheng: *Electrochim. Acta*, 2010, vol. 55, pp. 2498–2504.
52. N. Sato: *Corros. Sci.*, 1990, vol. 31, pp. 1–19.
53. N. Srinivasan, V. Kain, N. Birbilis, B.S. Kumar, M. Gandhi, P. Sivaprasad, G. Chai, A. Lodh, P. Ahmedabadi, and I. Samajdar: *Corros. Sci.*, 2016, vol. 111, pp. 404–13.
54. N.T. McDevitt and W.L. Baun: *Spectrochim. Acta*, 1964, vol. 20, pp. 799–808.
55. N. Srinivasan, B.S. Kumar, V. Kain, N. Birbilis, S. Joshi, P. Sivaprasad, G. Chai, A. Durgaprasad, S. Bhattacharya, and I. Samajdar: *Metall. Mater. Trans. A*, 2018, vol. 49A, pp. 2281–92.
56. J.O. Andersson, T. Helander, L. Höglund, P. Shi, and B. Sundman: *Calphad*, 2002, vol. 26, pp. 273–312.
57. L. da Costa Morais and R. Magnabosco: *Calphad*, 2017, vol. 58, pp. 214–18.
58. S. Wessman and R. Pettersson: *Steel Res. Int.*, 2015, vol. 86, pp. 1339–49.
59. J. Pospiech, K. Sztwiertnia, and F. Haessner: *Texture Stress Microstruct.*, 1986, vol. 6, pp. 201–15.
60. V. Randle and O. Engler: *Introduction to Texture Analysis: Macrotexture, Microtexture and Orientation Mapping*, CRC Press, Boca Raton, 2014.
61. M. Miodownik, A. Godfrey, E. Holm, and D. Hughes: *Acta Mater.*, 1999, vol. 47, pp. 2661–68.
62. P.J. Goodhew, J. Humphreys, and R. Beanland: *Electron Microscopy and Analysis*, CRC Press, Boca Raton, 2014.
63. S. Atamert and J. King: *Acta Metall. Mater.*, 1991, vol. 39, pp. 273–85.
64. H. Vannevik, J.O. Nilsson, J. Frodigh, and P. Kangas: *ISIJ Int.*, 1996, vol. 36, pp. 807–12.
65. L. Weber and P. Uggowitzer: *Mater. Sci. Eng. A*, 1998, vol. 242, pp. 222–29.
66. M.H. Jang, J. Moon, T.H. Lee, S.J. Park, and H.N. Han: *Metall. Mater. Trans. A*, 2014, vol. 45A, pp. 1653–58.
67. A. Mandal, S. Patra, D. Chakrabarti, and S.B. Singh: *Metall. Mater. Trans. A*, 2017, vol. 48A, pp. 5960–77.
68. N. Pettersson, S. Wessman, S. Hertzman, and A. Studer: *Metall. Mater. Trans. A*, 2017, vol. 48A, pp. 1562–71.
69. E. McCafferty: *Corros. Sci.*, 2005, vol. 47, pp. 3202–15.
70. K. Morshed-Behbahani, P. Najafisayar, M. Pakshir, and N. Zakerin: *Corros. Eng. Sci. Technol.*, 2019, vol. 54, pp. 174–83.
71. M. Ebrahimi, I. Danaee, H. Eskandari, and S. Nikmanesh: *IJSSSI*, 2017, vol. 14, pp. 9–15.
72. M. Carmezim, A. Simoes, M. Montemor, and M.D.C. Belo: *Corros. Sci.*, 2005, vol. 47, pp. 581–91.
73. X. Cheng, Y. Wang, X. Li, and C. Dong: *J. Mater. Sci. Technol.*, 2018, vol. 34, pp. 2140–48.
74. Z. Wang, L. Zhang, X. Tang, Z.Y. Cui, J.P. Xue, and M.X. Lu: *Int. J. Min. Met. Mater.*, 2017, vol. 24, pp. 943–53.
75. H.M. Cobb: *The History of Stainless Steel*, ASM International, Cleveland, 2010.
76. B. Leffler: *STAINLESS—Stainless Steels and Their Properties*, 1998, vol. 45. <https://www.outokumpu.com/files/group/hr/documents/stainless20.pdf>.
77. L. Guo, M. Li, X.L. Shi, Y. Yan, X. Li, and L. Qiao: *Corros. Sci.*, 2011, vol. 53, pp. 3733–41.
78. P.O. Malta, B.L. Condé, R.F. Assumpção, D.B. Perasoli, D.C. Sicupira, and D.B. Santos: *Metall. Mater. Trans. A*, 2019, vol. 50A, pp. 2665–77.
79. E. Symiotis: *Corrosion*, 1990, vol. 46, pp. 2–12.
80. M. Femenia: *Corrosion Behavior of Duplex Stainless Steels in Acidic-Chloride Solutions Studied with Micrometer Resolution*, Division of Corrosion Science, Royal Institute of Technology, Stockholm, 2003.
81. X. Wang and D. Li: *Electrochim. Acta*, 2002, vol. 47, pp. 3939–47.
82. A. Di Schino and J. Kenny: *J. Mater. Sci. Lett.*, 2002, vol. 21, pp. 1631–34.

83. K. Sugimoto and Y. Sawada: *Corros. Sci.*, 1977, vol. 17, pp. 425–45.
84. K. Hashimoto, K. Asami, and K. Teramoto: *Corros. Sci.*, 1979, vol. 19, pp. 3–14.
85. K. Hashimoto, K. Asami, A. Kawashima, H. Habazaki, and E. Akiyama: *Corros. Sci.*, 2007, vol. 49, pp. 42–52.

86. E. Rahimi, A. Kosari, S. Hosseinpou, A. Davoodi, H. Zandbergen, and J.M. Mol: *Appl. Surf. Sci.*, 2019, vol. 496, p. 143634.

Publisher's Note Springer Nature remains neutral with regard to jurisdictional claims in published maps and institutional affiliations.